Nonlinear Phenomena in Complex Systems, vol. **11**, no. 2 (2008), pp. 250 - 258

Dissipative Discrete Breathers in rf SQUID Metamaterials

N. Lazarides,* G. P. Tsironis, and M. Eleftheriou†
Department of Physics, University of Crete, and Institute of Electronic Structure and Laser, Foundation for Research and Technology-Hellas, P. O. Box 2208, 71003 Heraklion, GREECE
(Received 5 December, 2007)

The existence and stability of dissipative discrete breathers (DDBs) in rf superconducting quantum interference device (SQUID) arrays in both one and two dimensions is investigated numerically. In an rf SQUID array, the nonlinearity which is intrinsic to each SQUID due to the presence of the Josephson junction (on-site nonlinearity), along with the weak coupling of each SQUID to its nearest neighbors through magnetic forces, results in the appearance of discrete breathers. We analyze several discrete breather excitations, both in one and two dimensions, which are subjected to unavoidable losses. These losses, however, are counter-balanced by an external flux source leading to linearly stable discrete breather structures up to relatively large coupling parameters. We show that DDB excitations may locally alter the magnetic response of array from paramagnetic to diamagnetic or vice versa, and that they are not destroyed by increasing the dimensionality.

PACS numbers: 75.30.Kz, 74.25.Ha, 82.25.Dq, 63.20.Pw, 75.30.Kz, 78.20.Ci
Keywords: nonlinear magnetic metamaterials, rf SQUID array, discrete breathers

1. Introduction

Discrete breathers (DBs), also known as intrinsic localized modes (ILMs), are spatially localized, time-periodic, and stable (or at least long-lived) excitations in spatially extended, periodic, discrete, nonlinear systems [1, 2]. They can be produced spontaneously in a nonlinear lattice of weakly coupled elements as a result of fluctuations [3, 4], disordered [5], or by purely deterministic mechanisms [6, 7]. Since their introduction [8], a large volume of analytical and numerical studies have explored the existence and the properties of DBs in a variety of nonlinear mathematical models of physical systems. Rigorous mathematical proofs of existence of DBs in both energy conserved and dissipative lattices have been given [9, 10], and numerical algorithms for their numerically exact construction have been designed [11–16]. They have been observed experimentally in a variety of physical systems, including solid state mixed-valence transition metal complexes [17], quasi-one dimensional antiferromagnetic chains [18], arrays of Josephson junctions [19], micromechanical oscillators [20], optical waveguide systems [21], layered crystal insulator at $300K$ [22], and proteins [23].

From the perspective of applications to experimental situations where an excitation is subjected to dissipation and external driving, dissipative DBs (DDBs) are more relevant than their Hamiltonian (i.e., energy conserved) counterparts. Clearly, the dynamics of DDBs is governed by power balance, rather than energy conservation. In that case, quasiperiodic and even chaotic DDBs may exist [24, 25]. Recently, DDBs have been demonstrated numerically in discrete and nonlinear magnetic metamaterials (MMs) in both one and two dimensions [26, 27]. The MMs are artificial, composite, inherently non-magnetic materials that exhibit electromagnetic (EM) properties not available in naturally occurring materials. They are typically made of subwavelength resonant elements like, for example, the split-ring resonator. When driven by an alternating EM field, the MMs exhibit large magnetic response, either positive or negative, at frequencies ranging from the microwave up to the Terahertz (THz) and the optical bands [28–30]. Only a few natural materials respond magnetically at those frequencies, and that response is usually very weak and within a very narrow band. Thus, the magnetic response of materials at THz and optical frequencies is particularly important for the implementation of devices such as compact cavities, tunable mirrors, isolators, and converters. The negative response of MMs can be achieved above the resonance frequency, resulting in an effectively negative value of the magnetic permeability μ, the macroscopic parameter characterizing the magnetic response of a system. In a linear MM, the effective permeability μ does not depend on the intensity of the propagating EM field.

In contrast to the linear case, the effective parameters of MMs do depend on the intensity of the propagating EM field. Thus, the nonlinearity offers the possibility to achieve dynamic control over the effective parameters of a MM in real time, and thus tuning its properties by changing the intensity of that field. It has been recently suggested that periodic rf SQUID arrays can operate as nonlinear MMs in microwaves, due to the resonant nature of the SQUID itself and the nonlinearity inherent in the Josephson element. In that case, the effective μ of the rf SQUID array can be tuned by the applied

*Also at Department of Electrical Engineering, Technological Educational Institute of Crete, P. O. Box 140, Stavromenos, 71500, Heraklion, Crete, GREECE
†Also at Department of Music Technology and Acoustics, Technological Educational Institute of Crete, E. Daskalaki, Perivolia, 74100 Rethymno, Crete, GREECE

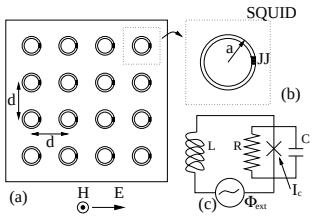

FIG. 1. Schematic drawing of the rf SQUID array, along with the equivalent circuit for a single rf SQUID in external alternating flux Φ_{ext}.

flux [31]. The combined effects of nonlinearity and discreteness (also inherent in rf SQUID arrays), may lead in the generation of nonlinear excitations in the form of DDBs. In the present context of MMs, such highly localized modes may alter locally the magnetic response of those materials [27].

In the present work we investigate numerically the existence and stability of DDBs in both one dimensional (1D) and two-dimensional (2D) arrays of rf superconducting quantum interference devices (SQUIDs). In the next section we describe the two-dimensional rf SQUID array model which consists a simple realization of a planar MM, while in section III we discuss its linear dispersion properties. In section IV we construct and present several types of DDBs both in one and two dimensions. In section V we shortly discuss the magnetic response of the rf SQUID arrays, showing that DDBs can locally alter the magnetic response from paramagnetic to diamagnetic (or vice versa). We finish in section VI with the conclusions.

2. rf SQUID array model

An rf SQUID, shown schematically in Fig. 1b, consists of a superconducting ring interrupted by a Josephson junction (JJ) [32, 33]. When driven by an alternating magnetic field, the induced supercurrents in the ring are determined by the JJ through the celebrated Josephson relations [34]. Adopting the resistively and capacitively shunted junction (RCSJ) model for the JJ [32, 33], an rf SQUID in an alternating magnetic field $H_{ext} \equiv H$ perpendicular to its plane is equivalent to the lumped circuit model shown in Fig. 1c. That circuit consists of an inductance L in series with an ideal Josephson element I_c (i.e., for which $I = I_c \sin\phi$, where I_c is the critical current of the JJ and ϕ is the Josephson phase) shunted by a capacitor C and a resistor R, driven by an alternating flux $\Phi_{ext}(H)$. The rf SQUID is a nonlinear oscillator which, in an alternating magnetic field exhibits a resonant magnetic response at a particular frequency $\omega_0 \simeq 1/\sqrt{LC} = \omega_p/\sqrt{\beta_L}$ (for $R \to \infty$), where ω_p is the plasma frequency of the JJ and $\beta_L = 2\pi L I_c/\Phi_0$ is the SQUID parameter (with Φ_0 being the flux quantum).

Consider a planar rf SQUID array consisting of identical units as shown in Fig. 1a, arranged in an orthogonal lattice with constants d_x and d_y in the x and y directions, respectively. That system is placed in a spatially uniform magnetic field $H = H_0 \sin(\omega t)$ of amplitude H_0 and frequency ω (t is the time variable), perpendicular to the SQUID rings. The field induces a supercurrent I_{nm} in the nmth SQUIDs through the flux $\Phi_{ext} = \Phi_{e0} \sin(\omega t)$ threading the SQUID loop ($\Phi_{e0} = \mu_0 S H_0 \omega$, where μ_0 is the permeability of the vacuum and S the loop area of the SQUID). The supercurrent I_{nm} produces a magnetic field which couples that SQUID with all the others due to magnetic dipole-dipole interactions through their mutual inductances. The behavior of that magneto-inductively coupled SQUID array is expected to deviate significantly from directly coupled SQUID arrays like, e.g. those studied in Ref. [35]. Assuming ring-shaped rf SQUIDs of radius a (so that $S = \pi a^2$), and using nearest-neighbor coupling between them, the flux Φ_{nm} trapped in the $(n,m)-$th SQUID ring is given by

$$\Phi_{nm} = \Phi_{ext} + L\,[I_{nm} + \lambda_x(I_{n-1,m} + I_{n+1,m}) + \lambda_y(I_{n,m-1} + I_{n,m+1})], \quad (1)$$

where $\lambda_{x,y} \equiv M_{x,y}/L$ are the coupling constants between any two neighboring SQUIDs in the x and y directions, coupled through mutual inductances M_x and M_y, respectively. Both values of the M_x and M_y are negative due to the fact that the magnetic field generated by one SQUID crosses the neighboring SQUID in the opposite direction. The supercurrent I_{nm} in the $(n,m)-$th SQUID ring is given, within the RCSJ model, by

$$-I_{nm} = C\frac{d^2\Phi_{nm}}{dt^2} + \frac{1}{R}\frac{d\Phi_{nm}}{dt} + I_c \sin\left(2\pi\frac{\Phi_{nm}}{\Phi_0}\right). \quad (2)$$

Due to the planar array geometry and for sufficiently large separations d_x and d_y in the x and y directions, we may assume that $\lambda_x, \lambda_y << 1$, and the nearest neighbor approximation holds. For the same reasons, we may neglect in the dynamical equations governing the fluxes in the SQUIDs all those terms of higher order, i.e., terms of the form $\lambda_x\lambda_y$, λ_y^2, λ_x^2, etc.

Solving Eq. (1) for the current I_{nm} we get

$$I_{nm} = \frac{\Phi_{nm} - \Phi_{ext}}{L} - \lambda_x(I_{n-1,m} + I_{n+1,m}) - \lambda_y(I_{n,m-1} + I_{n,m+1}). \quad (3)$$

Then we substitute Eq. (3), written for the currents $I_{n\pm1,m}$ and $I_{n,m\pm1}$, back into itself. Omitting higher order terms in the couplings, we get after rearrangement

$$\Phi_{nm} = \Phi_{ext} + L\,I_{nm} + \lambda_x(\Phi_{n-1,m} + \Phi_{n+1,m} - 2\Phi_{ext}) + \lambda_y(\Phi_{n,m-1} + \Phi_{n,m+1} - 2\Phi_{ext}). \quad (4)$$

By replacing I_{nm} in the earlier equations from Eq. (2) we get

$$C\frac{d^2\Phi_{nm}}{dt^2}+\frac{1}{R}\frac{d\Phi_{nm}}{dt}+I_c\,\sin\left(2\pi\frac{\Phi_{nm}}{\Phi_0}\right)-\lambda_x(\Phi_{n-1,m}+\Phi_{n+1,m})-\lambda_y(\Phi_{n,m-1}+\Phi_{n,m+1})$$
$$=[1-2(\lambda_x+\lambda_y)]\Phi_{ext}. \tag{5}$$

Using the relations $f_{nm}=\Phi_{nm}/\Phi_0$, $f_{ext}=\Phi_{ext}/\Phi_0$, $\beta=\beta_L/2\pi\equiv LI_c/\Phi_0$, $\gamma=L\omega_0/R$, $\tau=\omega_0 t$, equations (5) can be written in the normalized form

$$\frac{d^2 f_{nm}}{d\tau^2}+\gamma\frac{df_{nm}}{d\tau}+f_{nm}+\beta\,\sin(2\pi f_{nm})-\lambda_x(f_{n-1,m}+f_{n+1,m})-\lambda_y(f_{n,m-1}+f_{n,m+1})$$
$$=[1-2(\lambda_x+\lambda_y)]f_{ext}. \tag{6}$$

Note that the time derivative of f_{nm} corresponds to the voltage v_{nm} across the JJ of the $(n,m)-$th rf SQUID, i.e.,

$$v_{nm}=\frac{df_{nm}}{d\tau}. \tag{7}$$

The small parameter γ actually represents all of the dissipation coupled to each rf SQUID, which may also include radiative losses [36]. Equations (5) can be also obtained from the Hamiltonian

$$H = e^{-t/\tau_C}\sum_{n,m}\frac{Q_{nm}^2}{2C}+e^{+t/\tau_C}\sum_{n,m}\left[\frac{1}{2L}(\Phi_{nm}-\Phi_{ext})^2-E_J\,\cos\left(2\pi\frac{\Phi_{nm}}{\Phi_0}\right)\right.$$
$$\left.-\frac{\lambda_x}{L}(\Phi_{nm}-\Phi_{ext})(\Phi_{n-1,m}-\Phi_{ext})-\frac{\lambda_y}{L}(\Phi_{nm}-\Phi_{ext})(\Phi_{n,m-1}-\Phi_{ext})\right], \tag{8}$$

where $E_J\equiv I_c\,\Phi_0/2\pi$ is the Josephson energy, $\tau_C=RC$, and

$$Q_{nm}=e^{+t/\tau_C}\,C\,\frac{d\Phi_{nm}}{dt} \tag{9}$$

is the canonical variable conjugate to Φ_{nm}, and represents the charge accumulating across the capacitance of the JJ of each rf SQUID. The Hamiltonian Eq. (8) is a generalization in the 2D lossy case of that in Refs. [37, 38] used in the context of quantum computation with rf SQUID qubits.

3. Single rf SQUID oscillator

The dynamic equation for a single rf SQUID is given from Eqs. (6) for $\lambda_x=\lambda_y=0$ and $f_{nm}\to f$

$$\frac{d^2 f}{d\tau^2}+\gamma\frac{df}{d\tau}+f+\beta\,\sin(2\pi f)=f_{ext}, \tag{10}$$

which has been studied extensively for more than two decades both in the hysteretic ($\beta_L>1$) and the non-hysteretic ($\beta_L<1$) regimes. The external driving f_{ext} can be any time-dependent function, which may also include a constant term. In the following, we assume that the external flux is of the form

$$f_{ext}=f_{DC}+f_{e0}\cos(\Omega\tau), \tag{11}$$

where $f_{e0}=\Phi_{e0}/\Phi_0$ and $f_{DC}=\Phi_{DC}/\Phi_0$, with Φ_{DC} being a constant (DC) flux resulting from a time-independent and spatially uniform magnetic field. The nonlinear dynamics of Eq. (10) with f_{ext} given by Eq. (11) (with or without the DC term) is very rich, exhibiting bifurcations and chaos in large portions of the parameter space [39–41].

The properties of rf SQUIDs in an alternating external field as a nonlinear resonant oscillator have been investigated experimentally both for in hysteretic and the nonhysteretic (dispersive) regimes [42–44]. The signal amplitude of the rf SQUID as a function of the frequency of the applied rf field exhibits a strong resonance at a specific frequency at (or close to) ω_0.

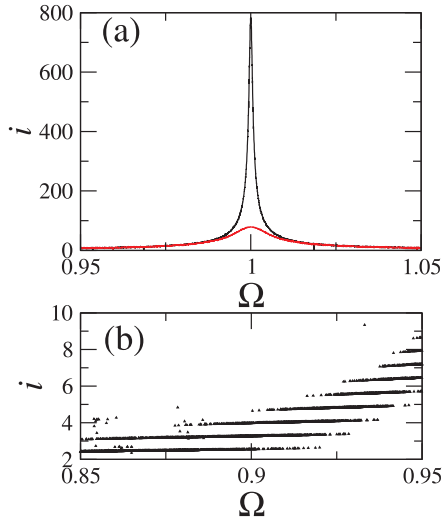

FIG. 2. (a) The resonance curve of the induced (super)current i as a function of the frequency of the applied rf field Ω for a single rf SQUID with $\beta = 1.27$, $f_{DC} = 0$, $f_{e0} = 1.0$, and $\gamma = 0.001$ (high peaked curve); $\gamma = 0.01$ (low peaked curve). (b) Enlargement of a small region from Fig. 2a where several fine steps on the resonance curve are clearly observable.

Although here we focus on the DDB generation in rf SQUID arrays, we shall refer shortly to the peculiar resonance behaviour of the single rf SQUID. A typical resonance curve for a hysteretic rf SQUID is shown in Fig. 2a, for two different values of the damping coefficient γ. Those symmetric, bell-shaped curves represent the flux amplitude of $f(\tau)$ as a function of the frequency ω of the applied field. Apparently, those curves have a maximum at $\omega = \omega_0$, and they are similar to those observed in high$-T_c$ rf SQUIDs in an alternating field (see for example figure 2d in Ref. [44]). Although these curves look smooth at first glance, they actually show multivalued behaviour, with jumps observed as fine steps as shown in Fig. Fig. 2b. For even lower rf power, however, we get very different resonance curves, as shown in Fig. 3. Here, instead of the symmetric curves of Fig. 2a, which are characteristic of linear resonance (in case we forget the fine steps), we see a curve with a hysteretic loop, which most closely resembles a typical nonlinear resonance curve. The hysteresis loops in Fig. 3 become smaller with increasing damping coefficient, as it could be expected. Thus, for such low rf powers, we can access the lowest energy states of the rf SQUID which actually are greatly affected by the nonlinearity. This behaviour is peculiar to the rf SQUID, where nonlinear effects are stronger for low applied power.

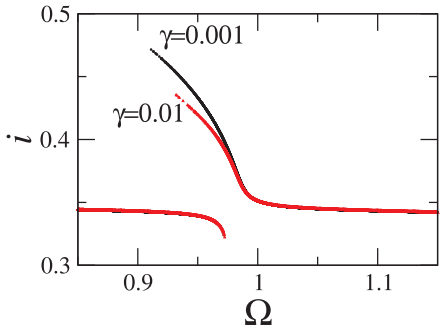

FIG. 3. The resonance curve of the induced (super)current i as a function of the frequency of the applied rf field Ω for a single rf SQUID with $\beta = 1.27$, $f_{DC} = 0$, $f_{e0} = 0.5$, and $\gamma = 0.001$ (high peaked curve); $\gamma = 0.01$ (low peaked curve). For such low rf power, the lowest energy but highly nonlinear state is accessed, which exhibits a typical nonlinear resonance curve with a hysteretic loop.

4. Linear dispersion

The linear dispersion for small amplitude flux waves is obtained by the substitution of $f = A \exp[i(\kappa_x n + \kappa_y m - \Omega\tau)]$, into the linearized Eq. (6) without losses and external field ($\gamma = 0$, $f_{ext} = 0$)

$$\Omega = \sqrt{1 + \beta_L - 2(\lambda_x \cos\kappa_x + \lambda_y \cos\kappa_y)}, \qquad (12)$$

where $\kappa_{x,y} = d_{x,y}\, k_{x,y}$ and $\Omega = \omega/\omega_0$. The earlier equation describes the dispersion of a new kind of guided waves, the magneto-inductive (MI) waves, which are supported by periodic, discrete arrays of magnetically coupled resonant elements [45]. Considering a 1D array, the corresponding dispersion (obtained by setting $\lambda_y = 0$ and dropping the subscript m) has similar form with that of electroinductive waves in chains of complementary metamaterial elements [46]. Moreover, in the limit of weak coupling ($\lambda_{x,y} \ll 1$), the dispersion (12) has similar form with that obtained for planar MI wave transducers, both in one [47] and two [45] dimensions. Typical $\Omega(\kappa)$ curves are shown in Fig. 4a for three different values of the coupling coefficient $\lambda = \lambda_x$. The bandwidth $\Delta\Omega \equiv \Omega_{max} - \Omega_{min}$ decreases with decreasing λ_x which leads, for realistic values of λ_x (between 0.05 and 0.1), to a nearly flat band with $\Delta\Omega \simeq 2\lambda\sqrt{1+\beta_L}$ (and relative bandwidth $\Delta\Omega/\Omega \simeq 2\lambda$). The corresponding phase and group velocities v_{ph} and v_g, respectively, for the red-dashed curve of Fig. 4a are shown in Fig. 4b. (Notice that the actual value of v_g has been multiplied by 250.) Importantly, the group velocity v_g, which defines the direction of power flow, is in a direction opposite to the phase velocity v_{ph}. Typical dispersion curves (i.e., contours of the

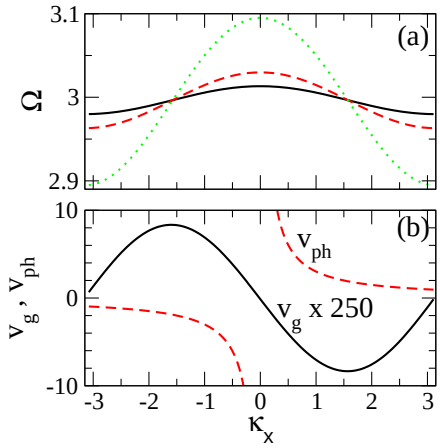

FIG. 4. (a) Frequency band Ω as a function of κ_x for a 1D rf SQUID array, for $\beta = 1.27$, and $\lambda_x = -0.05$ (narrowest band, black solid curve), $\lambda_x = -0.1$ (dashed curve), $\lambda_x = -0.3$ (widest band, dotted curve). (b) Group velocity v_g (solid curve) and phase velocity v_{ph} (dotted curve), for a 1D rf SQUID array with $\beta = 1.27$ and $\lambda_x = -0.1$.

frequency as a function of κ_x and κ_y) for both isotropic and anisotropic two-dimensional (2D) SQUID arrays are shown in Figs. 5a and 5b, respectively. In that case, v_g is not, in general, in a direction opposite to v_{ph}.

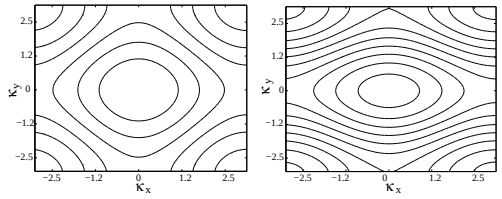

FIG. 5. Contours of the linear dispersion $\Omega_{\vec{\kappa}}$ in the $\kappa_x - \kappa_y$ plane for a two-dimensional rf SQUID array, with (i) $\lambda_x = -0.05$, $\lambda_y = -0.05$ (isotropic coupling); (ii) $\lambda_x = -0.05$, $\lambda_y = -0.10$ (anisotropic coupling). ($\beta = 1.27$).

5. Dissipative discrete breathers

Consider first the simpler case of a 1D finite rf SQUID array, consisting of N identical units. In order to generate DDBs we start by solving Eq. (6) in the anti-continuous limit [11], i.e., for $\lambda_x \equiv \lambda = 0$ when all SQUIDs are uncoupled. Then, the 1D Eqs. (6) reduce to Eq. (10), the equation for a single damped and driven rf SQUID [32]. We identify two different amplitude coexisting and stable attractors of the single rf SQUID oscillator, with flux amplitudes f_h and f_ℓ for the high and low amplitude attractor, respectively, and corresponding voltages v_h and v_ℓ,

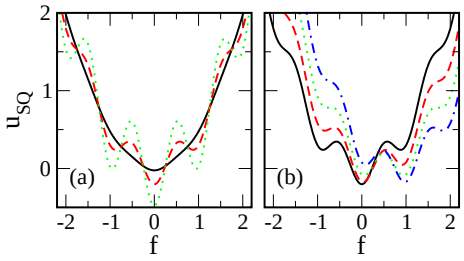

FIG. 6. Potential function of a single rf SQUID u_{SQ} as a function of its flux f, for (a) $f_{ext} = 0$, and $\beta = 0.15$ (solid curve), $\beta = 1.27$ (dashed curve), $\beta = 3$ (dotted curve); (b) $\beta = 1.27$, and $f_{ext} = 0$ (solid curve), $f_{ext} = 0.25$ (dashed curve), $f_{ext} = 0.5$ (dotted curve), $f_{ext} = 0.75$ (dashed-dotted curve).

respectively. Subsequently, we fix the flux amplitude and the voltage of one of the rf SQUIDs (say the one at $n = n_b = N/2$) to f_h and v_h, respectively, and all the others to f_ℓ and v_ℓ, respectively. Using this configuration (usually referred to as "trivial breather") as initial condition, we integrate the 1D Eqs. (6) for a sufficiently small value of $\lambda = \delta\lambda$. After integrating for a few hundred periods of the alternating driving field, the system has approached a stationary state. Then, we again increase λ by $\delta\lambda$ and start to integrate again the 1D Eqs. (6), using as initial condition the previously obtained stationary state. After integrating for a few more hundreds driving periods, the system has approached again a stationary state. Then, we increase again λ by $\delta\lambda$ and so on. Using this algorithm, we can construct DDBs up to some maximum value of the coupling λ [11]. For the integration of Eqs. (6) we use a standard fourth-order Runge-Kutta algorithm with fixed time-stepping Δt (typically $\Delta t = 0.01$). Since the DDBs presented here are highly localized, the choice of boundary conditions to be imposed on Eqs. (6) is not especially important. Thus, we have chosen periodic boundary conditions throughout the study. In the anti-continuous limit, all the SQUIDs are subjected to the same potential

$$u_{SQ} = \frac{1}{2}(f - f_{ext})^2 - \frac{\beta}{2\pi}\cos(2\pi f). \qquad (13)$$

Due to the form of u_{SQ} shown in Fig. 6, it is a rather obvious task to construct a "trivial breather i.e., a DDB for $\lambda_x = \lambda_y = 0$, when there are more than one local minimae. For example, when $\beta = 1.27$ and $f_{DC} = 0$ (read-dashed curve in Fig. 6a) one may choose the approximate values $f_\ell \simeq 0$ and $f_h \simeq 1$ (with $v_h = v_\ell \simeq 0$. These values lead to stable states of the single rf SQUID equation which are localized into the left and the right local minimae of the potential, respectively. Additionally, the choice of f_{e0} should be such that both those states will remain localize around the corresponding local minimum. By continuation of this trivial DDB for $\lambda_x, \lambda_y \neq 0$ one may obtain DDBs up to relatively high values of the coupling coefficients,

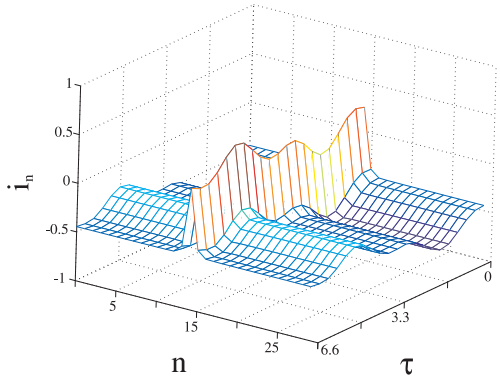

FIG. 7. Time evolution of a discrete dissipative breather during one period, for $f_{DC} = 0.5$, $f_{e0} = 0.2$, $\beta = 1.27$, $\alpha = 0.001$, $\lambda = 0.1$, and $T_b = 6.6$. Only part of the array ($N = 30$) is shown for clarity.

whose maximum depends on the specific value of f_{e0}. Such a DDB in a 1D rf SQUID array is shown in Fig. 7, where the spatio-temporal evolution of the induced currents i_n ($n = 1, 2, 3, ..., N$) are shown during one DDB period. Both the background and the central DDB site are oscillating with the same frequency $\Omega_b = 2\pi/T_b = \Omega$, i.e., a frequency equal to the driving frequency. We should also notice in Fig. 5 the non-sinusoidal time-dependence of the oscillations. When there are more than two local minimae in u_{SQ} (e.g., for $\beta = 3$, green-dotted curve in Fig. 6a) we can construct more than one different DDBs, by combining any two of the different coexisting and stable states. These DDBs are extremely stable, since they are constructed from stable and/or metastable (with very long life-time) localized states of u_{SQ}, which can survive down to zero frequencies. This is a characteristic example of a topological DDB. However, one can also construct DDBs whose central site crosses the zero level while oscillating. This requires the use of high amplitude states of the single rf SQUID oscillator, which may turn the SQUID into the normal (i.e., not superconducting) state. At that state, a rather large voltage difference appears along the JJ of that SQUID. Two typical examples of such DDBs, which may coexist, are shown in Fig. 8. Both the background and the central DDB site oscillate with the same frequency but different amplitudes (low and high amplitude current oscillation, respectively). The frequency of the oscillations, and thus the DDB frequency Ω_b, is again equal to the driving frequency Ω ($\Omega_b = \Omega$). However, there is a difference between the phases of the oscillation between the background and the central DDB site which is almost π, and that has profound consequences in the local magnetic properties of the array (see below). Although here we present only one-site, bright dissipative DBs, we can construct, by choosing appropriate initial conditions, many different types of DDBs. The linear stability of DDBs is addressed through the eigenvalues of

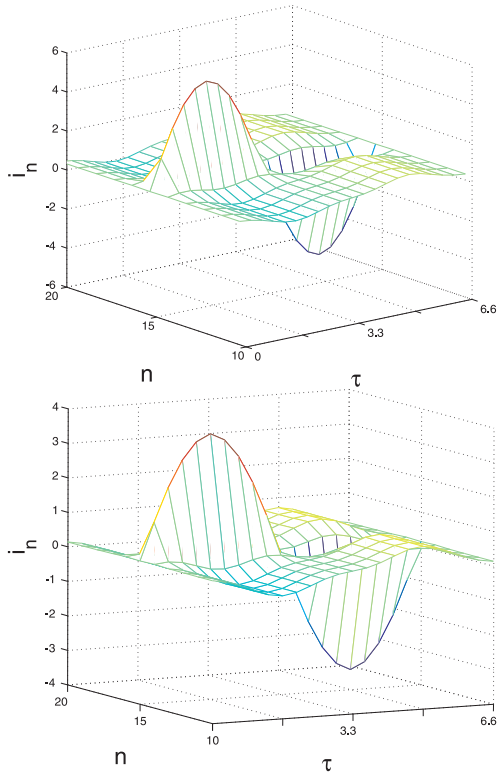

FIG. 8. Time evolution of two different discrete dissipative breathers during one period, for $f_{DC} = 0$, $f_{e0} = 0.6$, $\beta = 1.27$, $\alpha = 0.001$, $\lambda = 0.1$, and $T_b = 6.6$. Only part of the array ($N = 30$) is shown for clarity.

the Floquet matrix (Floquet multipliers). A DDB is linearly stable when all its Floquet multipliers m_i, $i = 1, ..., 2N$ lie on a circle of radius $R_e = \exp(-\alpha T_b/2)$ in the complex plane [12]. The DDBs shown in Figs. 7 and 8 (as well as those shown below), are all linearly stable. The calculated eigenvalues for the DDBs presented in Figs. and 8a and 8b are shown in the complex plane in Fig. 9a and 9b, respectively. Moreover, those DDBs were let to evolve for large time intervals (i.e., more than 10^5 T_b) without any observable change in their shapes.

We can also construct DDBs with periods which are multiple of the that of the external driver (subharmonic DDBs), for relatively weak coupling. Such a period-3 DDB, which is linearly stable, is shown in Fig. 10, while the Floquet spectrum of its eigenvalues is shown in Fig. 11a. In order to check directly its stability, this DDB was let to evolve for more than 5×10^5 T_b, without any observable change of its profile. We conclude, thus, that this period-3 DDB is stable, or at least that it is very long-lived. In

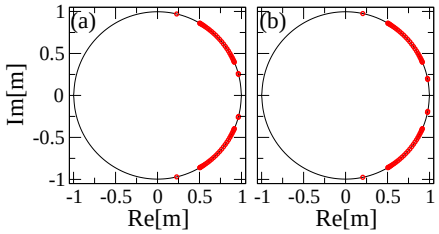

FIG. 9. Floquet spectra for the one-site bright dissipative breathers shown in (a) the upper panel of Fig. 6; and (b) the lower panel of Fig. 6. All eigenvalues lie on a circle of radius $R_e = \exp(-\alpha T_b/2) \simeq 0.996705$ in the complex plane.

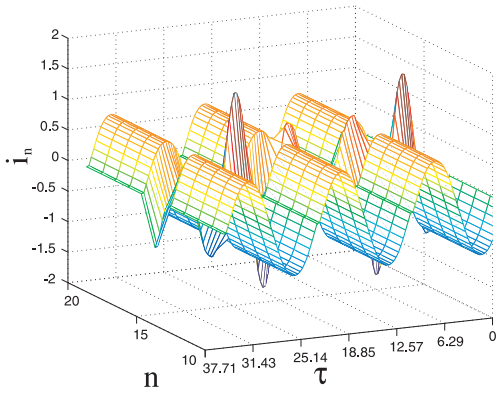

FIG. 10. Time evolution of a discrete, dissipative, period-3 breather during three driver periods, for $f_{DC} = 0$, $f_{e0} = 1.2$, $\beta = 1.27$, $\alpha = 0.001$, $\lambda = 0.0225$, and $T_b = 12.57$. Only part of the simulated array ($N = 30$) is shown for clarity.

Fig. 11b we show the Poincaré diagram (i.e., a diagram of f_n vs. $v_n = df_n/d\tau$ at the end of each period of the driver), for the central DDB site ($n = n_b = N/2$), as well as the site at $n = 7$ which is located in the background. Clearly, the trajectory of the central DDB site crosses the Poincaré surface at three points (red circles), while that of the site in the background at one point (black square).

Most of the methodology and techniques for DB construction has been developed for the 1D case. However, a rigorous proof of the existence of DBs in higher-dimensional nonlinear lattices was given in [9], and several numerical studies of DBs in 2D nonlinear lattices have been published [48–51]. Since rf SQUID arrays are fabricated in planar (2D) technology, it is necessary to extend the study of MI-DDBs in these systems in two dimensions. We have seen that DDBs are not destroyed by increasing the dimensionality from one to two. Consider a 2D $N \times N$ rf SQUID array consisting of identical units. Following the same procedure that we used to construct one-dimensional DDBs, we start from the anti-continuous limit by solving the single rf SQUID equation with losses

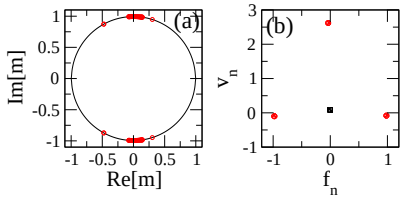

FIG. 11. (a) Floquet spectra for the one-site bright, dissipative, period-3 breather shown in fig. 8; all eigenvalues are in a circle of radius $R_e = \exp(-\alpha T_b/2) \simeq 0.993735$. (b) Poincaré surface of section for the central DB site at $n = n_b$ (red circles), and the site at $n = 7$ located in the background (black square), of the period-3 breather shown in fig. 8.

and a driving term of the form of Eq. (11). We identify two different coexisting and stable attractors of that oscillator with flux amplitudes f_h and f_ℓ and corresponding voltages v_h and v_ℓ, respectively. Then, in order to construct a trivial breather, we fix the flux amplitude and voltage of one of the rf SQUIDs (say the one at $(n, m) = (n_b, n_b) = (N/2, N/2)$) to f_h and v_h, respectively, and all the others to f_ℓ and v_ℓ, respectively. Then we integrate the 2D system of Eqs. (6) while increasing simultaneously the coupling coefficients λ_x and λ_y in small steps, as it was described earlier. Using this algorithm we have constructed several DDBs for an isotropic rf SQUID array ($\lambda_x = \lambda_y = \lambda$), up to some maximum λ. A snapshot of such a typical 2D isotropic DDB profile (at maximum amplitude of the central site) is shown in Fig. 12, for the same parameters used to construct the one-dimensional DDB of the top panel of Fig. 8. Note that the coupling coefficients λ_x and λ_y may differ in magnitude leading to anisotropic rf SQUID arrays. We have also constructed DDBs in anisotropic 2D arrays where $\lambda_x \neq \lambda_y$ (not presented here), for a wide range of the anisotropy parameter λ_y/λ_x.

6. Magnetic response

It is apparent from Fig. 8 that the low and high amplitude current oscillators have different phases with respect to the applied magnetic field. Consequently, their magnetic response in that field is expected to be different. To see that, we cast the normalized Eq. (1) in the form

$$\beta\, i_{nm} = f_{nm}^{loc} - f_{ext}^{eff}\,, \tag{14}$$

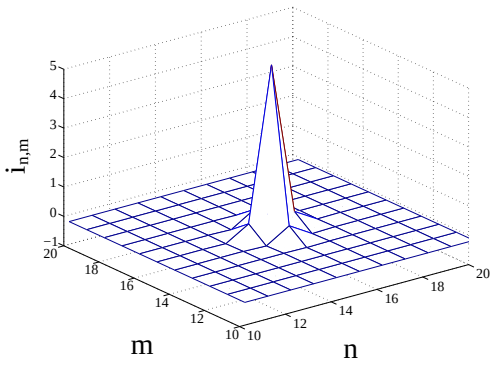

FIG. 12. A snapshot of a dissipative discrete breather (at maximum amplitude of the central site) for the parameters of fig. 6. Only part of the simulated array (30×30) is shown for clarity.

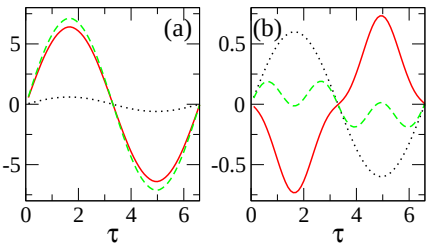

FIG. 13. Temporal evolution of the response βi_n (solid curve), the local flux f_n^{loc} (dashed curve), and the external flux f_{ext} (dotted curve) during one period T_b, for (a) the central site of the dissipative discrete breather shown in the top panel of Fig. 6 ($n = n_b = N/2$); (b) the site with $n = 7$ (which is located in the background) of the dissipative discrete breather shown in the top panel of Fig. 6 ($n = 7$).

where

$$f_{nm}^{loc} = f_{nm} - \lambda_x(f_{n-1,m} + f_{n+1,m}) - \lambda_y(f_{n,m-1} + f_{n,m+1}), \quad (15)$$

$$f_{ext}^{eff} = [1 - 2(\lambda_x + \lambda_y)]f_{ext}. \quad (16)$$

After division by the area of the unit cell d^2 of the 2D array, the terms f_{ext}^{eff}, f_{nm}^{loc}, and βi_{nm} in (14) can be interpreted as the effective external (driving) field, the local magnetic induction at cell (n, m), and the magnetic response (magnetization) at cell (n, m), respectively. Consider the DB shown in the top panel of Fig. 10. The temporal evolution (during one period) of βi_{nm}, f_{nm}^{loc}, and f_{ext}^{eff}, which are directly proportional to its magnetic response, the local magnetic induction, and the external magnetic field, respectively, are shown in Fig. 13 for two different cells of the array; the central (breather) cell at $(n, m) = (n_b, n_b)$, and the cell at $(n, m) = (7, 7)$ (Fig. 13a and Fig. 13b, respectively). The latter is chosen to lie in the oscillating background, relatively far from the central DDB site and the ends of the array. We observe significant differences in the magnetization (red-solid curves) in those two cells; in the cell containing the high current amplitude oscillator (i.e., the central DDB site) the magnetization is in phase with the applied field, while in the other cell the magnetization is in anti-phase with that. Thus, in the present case, the DDB provides a diamagnetic response in a strongly paramagnetic background. In this sense, a DDB may alter locally the character of the magnetic response (paramagnetic/diamagnetic) of a SQUID array in an alternating magnetic field. In some cases, the magnitude of the magnetization of the DDB may exceed that of the applied field, leading to extreme diamagnetic or negative magnetic response.

7. Conclusions

In conclusion, we have shown using standard numerical methods that both 1D and 2D periodic rf SQUID arrays in an alternating external flux support several types of linearly stable DDBs. Those arrays belong to the class of MI systems, since the individual rf SQUIDs are weakly coupled through magnetic interactions. Similar MI DDBs were found to exist also in arrays of split-ring resonators [26, 27], which constitute the most common elements for the construction of MMs. We speculate that DDBs generically exist in discrete and nonlinear MI systems, for rather wide parameter ranges, and they are linearly stable for weak coupling between their units. For the rf SQUID array we have also obtained different DDB excitations which may co-exist as well as multiperiodic DDBs, which are linearly stable. The latter are obtained only for relatively weak coupling between SQUIDs. Moreover, DDBs may alter locally the magnetization (magnetic response) of an rf SQUID array in an alternating magnetic field. The increasing of dimensionality does not, in general, destroy the DDB solutions. Thus, it seems possible to exploit dissipative multibreathers in order to create strongly paramagnetic "islands"in a 2D SQUID array, surrounded by a diamagnetic (or even extreme diamagnetic) background. The co-existence of several linearly stable DDB is a result of the rich nonlinear dynamics of single SQUIDs, which allows for multistability even for frequencies far from resonance. The weak coupling modifies only slightly the amplitude of oscillation of those states in each SQUID in the array. Thus, it is also possible to get a multiplicity of uniform solutions in a wide range of frequencies, which provide different magnetic responses (paramagnetic or diamagnetic).

Acknowledgements

We acknowledge support from the grant "Pythagoras II"(KA. 2102/TDY 25) of the Greek Ministry of Education and the European Union.

References

[1] S. Flach and C. R. Willis, Phys. Rep. **295**, 181 (1998).
[2] D. K. Campbell, S. Flach, and Y. S. Kivshar, Physics Today p. 43 (2004).
[3] M. Peyrard, Phys. D **119**, 184 (1998).
[4] K. Ø. Rasmussen, S. Aubry, A. R. Bishop, and G. P. Tsironis, Eur. Phys. J. B **15**, 169 (2000).
[5] K. Ø. Rasmussen, D. Cai, A. R. Bishop, and N. Grønbech-Jensen, Europhys. Lett. **47**, 421 (1999).
[6] D. Hennig, L. Schimansky-Geier, and P. Hänggi, Europhys. Lett. **78**, 20002 (2007).
[7] D. Hennig, S. Fugmann, L. Schimansky-Geier, and P. Hänggi, Phys. Rev. E **76**, 041110 (2007).
[8] A. J. Sievers and S. Takeno, Phys. Rev. Lett. **61**, 970 (1988).
[9] R. S. MacKay and S. Aubry, Nonlinearity **7**, 1623 (1994).
[10] S. Aubry, Phys. D **103**, 201 (1997).
[11] J. L. Marín and S. Aubry, Nonlinearity **9**, 1501 (1996).
[12] J. L. Marín, F. Falo, P. J. Martínez, and L. M. Floría, Phys. Rev. E **63**, 066603 (2001).
[13] D. Zueco, P. J. Martínez, L. M. Floría, and F. Falo, Phys. Rev. E **71**, 036613 (2005).
[14] G. P. Tsironis, J. Phys. A:Math. Gen. **35**, 951 (2002).
[15] J. M. Bergamin and T. Bountis, Prog. Theor. Phys. Suppl. **150**, 330 (2003).
[16] P. Panagopoulos, T. Bountis, and C. Skokos, J. Vib. Acoust. **126**, 520 (2004).
[17] B. I. Swanson, J. A. Brozik, S. P. Love, G. F. Strouse, A. P. Shreve, A. R. Bishop, W.-Z. Wang, and M. I. Salkola, Phys. Rev. Lett. **82**, 3288 (1999).
[18] U. T. Schwarz, L. Q. English, and A. J. Sievers, Phys. Rev. Lett. **83**, 223 (1999).
[19] E. Trías, J. J. Mazo, and T. P. Orlando, Phys. Rev. Lett. **84**, 741 (2000).
[20] M. Sato, B. E. Hubbard, A. J. Sievers, B. Ilic, D. A. Czaplewski, and H. G. Graighead, Phys. Rev. Lett. **90**, 044102 (2003).
[21] H. S. Eisenberg, Y. Silberberg, R. Morandotti, A. R. Boyd, and J. S. Aitchison, Phys. Rev. Lett. **81**, 3383 (1998).
[22] F. M. Russell and J. C. Eilbeck, Europhys. Lett. **78**, 10004 (2007).
[23] J. Edler, R. Pfister, V. Pouthier, C. Falvo, and P. Hamm, Phys. Rev. Lett. **93**, 106405 (2004).
[24] P. J. Martínez, L. M. Floría, F. Falo, and J. J. Mazo, Europhys. Lett. **45**, 444 (1999).
[25] P. Maniadis and T. Bountis, Phys. Rev. E **73**, 046211 (2006).
[26] N. Lazarides, M. Eleftheriou, and G. P. Tsironis, Phys. Rev. Lett. **97**, 157406 (2006).
[27] M. Eleftheriou, N. Lazarides, and G. P. Tsironis (2007).
[28] T. J. Yen, W. J. Padilla, N. Fang, D. C. Vier, D. R. Smith, J. B. Pendry, D. N. Basov, and X. Zhang, Science **303**, 1494 (2004).
[29] V. A. Podolskiy, A. K. Sarychev, and V. M. Shalaev, Opt. Express **11**, 735 (2003).
[30] C. M. Soukoulis, S. Linden, and M. Wegener, Science **315**, 47 (2007).
[31] N. Lazarides and G. P. Tsironis, Appl. Phys. Lett. **16**, 163501 (2007).
[32] K. K. Likharev., *Dynamics of Josephson Junctions and Circuits.* (Gordon and Breach, Philadelphia, 1986).
[33] A. Barone and G. Patternó., *Physics and Applications of the Josephson Effect.* (Wiley, New York, 1982).
[34] B. Josephson, Phys. Lett. A **1**, 251 (1962).
[35] D.-X. Chen, J. J. Moreno, A. Hernando, and A. Sanchez, Europhys. Lett. **41**, 413 (1998).
[36] I. Kourakis, N. Lazarides, and G. P. Tsironis, Phys. Rev. E **75**, 067601 (2007).
[37] T. Roscilde, V. Corato, B. Ruggiero, and P. Silvestrini, Phys. Lett. A **345**, 224 (2005).
[38] V. Corato, T. Roscilde, B. Ruggiero, C. Granata, and P. Silvestrini, J. Phys: Conf. Series **43**, 1401 (2006).
[39] M. P. Sørensen, M. Bartuccelli, P. L. Christiansen, and A. R. Bishop, Phys. Lett. A **109**, 347 (1985).
[40] R. K. Ritala and M. M. Salomaa, Phys. Rev. B **29**, 6143 (1984).
[41] K. Fesser, A. R. Bishop, and P. Kumar, Appl. Phys. Lett. **43**, 123 (1983).
[42] V. I. Shnyrkov, V. A. Khlus, and G. M. Choi, J. Low Temp. Phys. **39**, 447 (1980).
[43] I. M. Dmitrenko, G. M. Choi, V. I. Shnyrkov, and V. V. Kartsovnik, J. Low Temp. Phys. **49**, 417 (1982).
[44] X. H. Zeng, Y. Zhang, B. Chesca, K. Barthel, Y. S. Greenberg, and A. I. Braginski, J. Appl. Phys. **88**, 6781 (2000).
[45] R. R. A. Syms, E. Shamonina, and L. Solymar, Eur. Phys. J. B **46**, 301 (2005).
[46] M. Beruete, F. Falcone, M. J. Freire, R. Marqués, and J. D. Baena, Appl. Phys. Lett. **88**, 083503 (2006).
[47] M. J. Freire, R. Marqués, F. Medina, M. A. G. Laso, and F. Martín, Appl. Phys. Lett. **85**, 4439 (2004).
[48] S. Flach, K. Kladko, and S. Takeno, Phys. Rev. Lett. **79**, 4838 (1997).
[49] J. J. Mazo, Phys. Rev. Lett. **89**, 234101 (2002).
[50] V. M. Burlakov, S. A. Kiselev, and V. N. Pyrkov, Phys. Rev. B **42**, 4921 (1990).
[51] P. G. Kevrekidis, K. Ø. Rasmussen, and A. R. Bishop, Phys. Rev. E **61**, 2006 (2000).